# EVALUATION OF UV AEROSOL RETRIEVALS FROM AN OZONE LIDAR

Shi Kuang[1]*, Bo Wang[1], Michael J. Newchurch[1], Kevin Knupp[1], Paula Tucker[1], Edwin W. Eloranta[2], Joseph P. Garcia[2], Ilya Razenkov[2], John T. Sullivan[3], Timothy A. Berkoff[4], Guillaume Gronoff[4,5], Liqiao Lei[4,6], Christoph J. Senff[7,8], Andrew O. Langford[7], Thierry Leblanc[9], Vijay Natraj[10]

[1]University of Alabama in Huntsville, Huntsville, Alabama, USA

[2]University of Wisconsin-Madison, Madison, Wisconsin, USA

[3]NASA Goddard Space Flight Center, Greenbelt, Maryland, USA

[4]NASA Langley Research Center, Hampton, Virginia, USA

[5]Science Systems and Applications Inc., Lanham, Maryland, USA

[6]Universities Space Research Association, Columbia, Maryland, USA

[7]NOAA Earth System Research Laboratory, Boulder, Colorado, USA

[8]Cooperative Institute for Research in Environmental Sciences, University of Colorado, Boulder, Colorado, USA

[9]Jet Propulsion Laboratory, California Institute of Technology, Wrightwood, CA, USA

[10]Jet Propulsion Laboratory, California Institute of Technology, Pasadena, California, USA

*Correspondence to*: Shi Kuang (kuang@nsstc.uah.edu)

## Abstract

Aerosol retrieval using ozone lidars in the ultraviolet spectral region is challenging but necessary for correcting aerosol interference in ozone retrieval and for studying the ozone-aerosol correlations. This study describes the aerosol retrieval algorithm for a tropospheric ozone lidar, quantifies the retrieval error budget, and intercompares the aerosol retrieval products at 299 nm with those at 532 nm from a high spectral resolution lidar (HSRL) and with those at 340 nm from an Aerosol Robotic Network radiometer. After the cloud-contaminated data is filtered out, the aerosol backscatter or extinction coefficients at a 30-m and 10-min resolution retrieved by the ozone lidar are highly correlated with the HSRL products, with a coefficient of 0.95 suggesting that the ozone lidar can reliably measure aerosol structures with high spatio-temporal resolution when the signal-to-noise ratio is sufficient. The actual uncertainties of the aerosol retrieval from the ozone lidar generally agree with our theoretical analysis. The backscatter color ratio (backscatter-related exponent of wavelength dependence) linking the coincident data measured by the two instruments at 299 and 532 nm is $1.34 \pm 0.11$ while the Ångström (extinction-related) exponent is $1.49 \pm 0.16$ for a mixture of urban and fire smoke aerosols within the troposphere above Huntsville, AL, USA.

## 1. Introduction

A tropospheric ozone differential absorption lidar (DIAL) makes measurements of vertical ozone profiles, typically at two wavelengths chosen between 277 and 300 nm with a separation less than 12 nm, by weighing several parameters such as the ozone absorption cross sections, solar background, dynamic range of the detection system, and interference from aerosols and other species (e.g., Alvarez et al., 2011; Browell et al., 1985; De Young et al., 2017; Fukuchi et al.,

001; Kempfer et al., 1994; McDermid et al., 2002; Proffitt and Langford, 1997; Strawbridge et al., 2018; Sullivan et al., 2014). Vertical aerosol profiles are of high interest not only because they are needed for aerosol correction in ozone lidar retrievals (Steinbrecht and Carswell, 1994), but also because simultaneous ozone and aerosol vertical profile measurements provide unique information on their interactions and on sources of pollutant transport (Browell et al., 1994; Langford et al., 2020; Newell et al., 1999). However, there is currently no consensus on the reliability of the aerosol retrievals produced by ozone lidars due to the difficulty of solving the three-component lidar equation and the large variability in aerosol optical properties associated with the multiplicity of aerosol types and size distributions.

The most widely used solution for the elastic single-wavelength aerosol lidar equation is the analytic method developed by Klett (1981). The inversion method then inspired Fernald (1984) to publish a computer algorithm scheme to solve the more general two-component (aerosol and molecular) atmospheric lidar equation. The Klett (1981) inversion requires *a priori* for the lidar ratio (i.e., aerosol extinction-to-backscatter ratio, represented by "$S$" hereafter) to link the aerosol backscatter with its extinction for solving the lidar equation. Lasers used for aerosol lidars are preferred in the visible and infrared bands, typically 532 and 1064 nm for Nd:YAG laser or 694 nm for Ruby laser (Russell et al., 1979), where the ozone absorption is much smaller than molecular and Mie scattering. In the ultraviolet (UV) band for an ozone lidar, the ozone absorption may not be trivial. Some ozone lidars have an aerosol channel available, either independently or sharing receiving optics with the ozone channel (e.g., Browell et al., 1994; De Young et al., 2017; Gronoff et al., 2019; Kovalev and McElroy, 1994; Uchino and Tabata, 1991). For most of the traditional two-wavelength ozone lidars without an aerosol channel, although there has been some discussion about the aerosol retrieval algorithm (e.g., Eisele and Trickl, 2005; Langford et al., 2019; Papayannis et al., 1999; Sullivan et al., 2014), the evaluation of the aerosol retrieval product and its error budget have rarely been addressed. Due to a significant wavelength difference with aerosol lidars, several aspects of the aerosol retrieval using an ozone lidar are worth noting. First, the signal-to-noise ratio (SNR) for ozone lidars decays quicker with altitude due to more significant UV molecular (i.e., Rayleigh) scattering and ozone absorption resulting in a lower retrievable altitude than aerosol lidars. Second, since the molecular and ozone components become more important at UV wavelengths compared to visible and infrared wavelengths, the uncertainties in aerosol retrieval propagated from the calculation of these two components are expected to be larger for ozone lidars than for aerosol lidars. Third, $S$ and the wavelength dependence used for the ozone lidar wavelengths may be different from those used for the longer aerosol lidar wavelengths (Ackermann 1998; Eck et al., 1999).

The primary objectives of this article are to investigate the performance of our aerosol retrieval algorithm and to quantify its error budget for the ozone lidar. The secondary goal is to seek the overall wavelength dependence between the aerosol optical properties measured by the ozone lidar at 299 nm and by a high spectral resolution lidar (HSRL) at 532 nm.

## 2. Instruments and Data Processing

### 2.1. Ozone Lidar

The Rocket-city Ozone ($O_3$) Quality Evaluation in the Troposphere (RO$_3$QET) lidar is located on the campus of the University of Alabama in Huntsville (UAH) at 34.725 ˚N and 86.645 ˚W at 206 m asl and is one of the six systems of the Tropospheric Ozone Lidar Network (TOLNet) (http://www-air.larc.nasa.gov/missions/TOLNet). This system

74  measures ozone from 0.1 km up to about 12 km during nighttime and up to about 6 km during daytime with a temporal

75  resolution of 2 min. The vertical resolution of the lidar retrievals varies from 150 m in the lower troposphere to 750

76  m in the upper troposphere in order to keep the measurement uncertainty within ±10% (Kuang et al., 2013).

77  The transmitter comprises two Raman-shifted lasers at 289 and 299 nm. Two 30-Hz, 266-nm Nd:YAG lasers

78  pump two 1.8-m Raman cells, respectively, with mixtures of active gas and buffer gas to generate 289 and 299-nm

79  lasers with an average pulse energy of about 5 mJ. The receiving system consists of three receivers with diameters of

80  2.5 cm, 10 cm, and 40 cm, respectively, and four photomultipliers (PMTs) similar to that described by Kuang et al.

81  (2013) except that the solar filters have been replaced by 300-nm short-pass filters for all telescopes. Channels-1, 2,

82  3, 4 represent the 2.5-cm, 10% of the 10-cm, 90% of the 10-cm, and the 40-cm telescope channels, respectively. Since

83  the modification of Channel–4 through the addition of narrow-band solar filters was not completed before the time

84  period of this study, data from this channel was not used in this work, with the net result that uncertainties for ozone

85  retrievals above 6 km during daytime were often too large due to the strong solar background. Lidar signal counting

86  was accomplished by four Licel transient recorders (Licel company, Germany) with both analog and photoncounting

87  (PC) modes, with a sampling rate of 40 MHz corresponding to a 3.75-m fundamental resolution. The cloud base height

88  is determined by the following empirical method. Derivatives of the logarithm of the off-line analog signal are

89  calculated for a lidar signal profile and the first range bin at which the derivative is greater than a certain threshold is

90  considered to be the cloud base height. The threshold is chosen empirically based on the lidar SNR and the vertical

91  resolution. Therefore, lidar data with cloud base lower than 2 km was discarded. The cloud filtering process should

92  be conducted carefully because an elastic lidar without a polarization channel is not capable of accurately

93  distinguishing aerosols and clouds solely through their backscatter properties. Five 2-min lidar data intervals were

94  combined to give a 10-min lidar-signal integration time to improve the SNR. Further, six of the 3.75-m fundamental

95  bins were integrated for all channels. In addition, dead-time correction (for PC signal only), background correction,

96  analog-PC signal merging, and signal-induced noise correction were performed.

97  **2.2.    Aerosol Retrieval and Uncertainty Estimation**

98  The aerosol profiles were retrieved with an iterative DIAL algorithm. A brief description of this algorithm is

99  provided in this section, with further details in Appendix A. A first-order Savitzky-Golay differentiation filter with a

100  second-degree polynomial was applied to the logarithm of the signal ratios to compute the first-cut ozone profile. This

101  initial ozone profile was substituted back into the three-component lidar equation to derive the profile of aerosol

102  backscatter coefficients at 299 nm by assuming a constant $S$ of 60 sr and boundary value of the aerosol backscatter

103  coefficient at a far-range reference altitude, about 10 km. During the daytime, the ozone retrieval was limited by the

104  lower SNR of the 289-nm channel, but the 299-nm channel had much better SNR due to lower atmospheric extinction

105  and was able to measure aerosol up to higher altitudes. $S$ has large variability as a function of aerosol characteristics,

106  humidity, and wavelength (Ackermann, 1998; Strawbridge et al., 2018; Mishchenko et al., 1997). The $S$ *a priori* value

107  assumed for this study represents a mix of urban and smoke aerosols during the lidar observations (Ackermann, 1998;

108  Burton et al., 2012; Cattrall et al., 2005; Groß et al., 2013; Müller et al., 2007). The *a priori* is application dependent.

109  In the aerosol retrieval uncertainty discussion in Appendix B, we assume a ±20% uncertainty for $S$ based on an average

110  standard deviation obtained from prior observations (Müller et al., 2007).

111    Molecular backscatter and extinction profiles were computed from local radiosonde data. Then, the aerosol

112    profile was substituted into the lidar equation again to obtain a stable solution, usually within three iterations. This

113    aerosol profile was further employed to calculate the aerosol correction for ozone retrievals using the first-order Taylor

114    approximation (Browell et al., 1985) by assuming a power law wavelength dependence for the aerosol extinction and

115    choosing an appropriate Ångström exponent. Since this work focuses only on aerosol retrieval, details of the ozone

116    correction will be described in a future article. Finally, the aerosol profiles derived by the three altitude channels were

117    merged into a single profile in the overlapping altitude zones, i.e., 0.5–1 km for Channels-1 and 2 and 1.5–2 km for

118    Channels-2 and 3.

119    The primary uncertainty sources for the aerosol lidar retrievals are the uncertainties in lidar signal

120    measurement, boundary value assumption for aerosol backscatter coefficient, air density measurement, $S$ *a priori*, and

121    ozone profile input. The relative importance of these sources is altitude dependent. In the planetary boundary layer

122    (PBL) where the air is typically turbid, the $S$ uncertainty is dominant while other sources are minor (only few percent).

123    The uncertainty of $S$ influences the uncertainty of the aerosol backscatter through a complicated relationship. However,

124    the magnitude of the above two uncertainties can be approximately seen to be close. At the far range (higher than 7

125    km), lidar signal detection noise and inaccurate boundary value assumption are important. Influence from both of the

126    above sources, especially the boundary value, on the aerosol retrieval quickly decreases towards the ground from the

127    far range. In the middle range (PBL top – 7 km), both the air density measurement error and lidar signal detection

128    noise are essential. Uncertainty due to ozone profile input is relatively unimportant and is only few percent at most

129    altitudes. Figure B1 presents an example of the aerosol backscatter uncertainty calculated from 10-min nighttime

130    RO$_3$QET lidar data. The error budget estimate generally justifies the choice of using 6 km as the maximum altitude

131    for RO$_3$QET-HSRL comparison since the total uncertainty for the RO$_3$QET aerosol retrieval could be unacceptably

132    large (i.e., persistently larger than 100%).

133    **2.3.    HSRL**

134    The University of Wisconsin HSRL (Eloranta, 2005) was deployed in Huntsville, AL from 19 June to 4 November

135    2013 and operated almost 24 hours every day to support the Studies of Emissions and Atmospheric Composition,

136    Clouds and Climate Coupling by Regional Surveys SEAC[4]RS campaign (Kuang et al., 2017). The HSRL transmitter

137    was a diode-pumped Nd:YAG laser at 532 nm with a pulse energy of about 50 μJ and a pulse repetition frequency of

138    4 kHz. The expanded laser beam was transmitted coaxially with a 40-cm telescope with a tiny field of view (FOV) of

139    100 μrad to reduce solar background. The HSRL spectral filtering can separate the molecular backscatter from the

140    aerosol backscatter due to the molecular Doppler broadening effect while the particulate backscatter remains spectrally

141    unbroadened. Aerosol backscatter coefficients can then be calculated as the difference between the total return and

142    the molecular component (Grund and Eloranta, 1991). In principle, aerosol extinction can also be computed by

143    comparing the measured attenuated molecular backscatter to a reference, unattenuated molecular backscatter profile

144    that is calculated from radiosonde-measured air density profile or a numerical model (Hair et al., 2008). However,

145    small and fast signal fluctuations were found in the partial overlap region (between the surface and about 4.5 km) for

146    the data taken in Huntsville so that aerosol extinction below 4.5 km cannot be derived with a satisfying precision. The

147    signal fluctuations were probably caused by small optical misalignments from temperature changes within the lidar

148 system (Reid, et al., 2017). The aerosol backscatter calculation is not affected by the lidar signal fluctuations since

149 any range-dependent instrument effects are canceled out. Therefore, we focus on the aerosol backscatter

150 intercomparison between the HSRL and RO$_3$QET. If aerosol extinction is needed for the HSRL, we will calculate it

151 from the aerosol backscatter by assuming a constant lidar ratio. The HSRL provides aerosol products with a 30-m

152 vertical resolution and 1-min temporal resolution from near the surface to 15 km. To achieve sufficient SNR for both

153 HSRL and ozone lidar and to reduce the uncertainty arising from the clock bias of the controlling computers, we adopt

154 10-min temporal average and 30-m vertical average for both HSRL and ozone lidar in the intercomparison study. The

155 HSRL has a backscatter measurement precision better than $10^{-7}$ (m sr)$^{-1}$ for a 1-min signal average (Reid et al., 2017),

156 which represents an estimated precision for the extinction coefficient of better than $2 \times 10^{-6}$ m$^{-1}$ for a 10-min average.

157 **3.    Intercomparison Results**

158 We select four time periods (21–23 June, 14–15 August, 27–28 August, and 5–6 September, 2013) to investigate the

159 ozone lidar capability for measuring aerosol column and range-resolved profiles. All four cases have coincident ozone

160 lidar and HSRL observation periods longer than 24 hours, fully covering the convective mixing layer development

161 and collapse processes (Klein et al., 2019) and having significant smoke layers in the free troposphere. Due to the

162 significant extinction and potential multiple scattering caused by clouds, the ozone lidar is incapable of measuring

163 either ozone or aerosol accurately above clouds, especially thick clouds. Therefore, data contaminated by clouds is

164 filtered out. At this time, the narrow-band interference filters had not been incorporated into the receiving system and

165 the wide-band filter resulted in substantial solar background during the daytime; hence, we set 6 km asl as the

166 maximum altitude for intercomparison. The uncertainty of the aerosol retrieval owing to lidar signal measurement

167 error is dominant at far range and is determined by the lidar SNR, as shown in Appendix B.2. The solar background

168 is an important noise resulting in the lidar signal measurement error during daytime and is partly responsible for the

169 high aerosol retrieval uncertainty above 6 km as shown by the example in Figure B1. The 10-min HSRL profiles are

170 interpolated to the times of the ozone lidar data.

171        First, we investigate the correlation of the integrated (or column) aerosol backscatter between the ozone lidar

172 and HSRL to obtain a general relationship between their averages. Figure 1 shows that the RO$_3$QET- and HSRL-

173 derived integrated backscatter coefficients for all four cases are highly correlated, with a Pearson correlation

174 coefficient of 0.99. The root mean square error (RMSE), the standard deviation of the residuals, is negligibly small at

175 $1 \times 10^{-3}$ sr$^{-1}$, suggesting that the linear regression equation can accurately represent the relationship between the AOD

176 measured by the two instruments. The 493 sampling profiles cover 82 hours of coincident ozone lidar and HSRL

177 observations. We define the aerosol backscatter color ratio (å$_\beta$) as (Burton et al., 2012):

$$178 \qquad \mathring{a}_\beta = -\frac{d(ln\beta_A)}{d(ln\lambda)} = -\frac{ln\left(\frac{\beta_A^{299}}{\beta_A^{532}}\right)}{ln\left(\frac{299}{532}\right)}, \qquad\qquad (1)$$

179 where $\beta_A^{299}$ and $\beta_A^{532}$ represent the aerosol backscatter coefficient at 299 and 532 nm, respectively. The subscript "*A*"

180 represents the "aerosol" component, to be distinguished from the "molecular" contribution that is represented by

181 subscript "*M*" in the Appendix. å$_\beta$ is an exponent denoting backscatter-related wavelength dependence, to be

182 distinguished from the commonly-used Ångström exponent (Ångström, 1929) that refers to the wavelength

183 dependence of optical thickness or extinction coefficient. å$_\beta$ is also different from another often-used concept, "color

184    ratio of the lidar ratios", which refers to the ratio of $S$ at two different wavelengths. The slope of the regression, equal

185    to 2.16, results in the best least-squares fit value of 1.34 for $\text{å}_\beta$ at 299 and 532 nm. The uncertainty of the column $\beta_A^{299}$

186    is expected to be smaller than the uncertainty for $\beta_A^{299}$ at a particular altitude and for a 10-min integration time (in

187    Figure B1) since the average over longer time and altitude range greatly reduces the random noise as suggested by the

188    small RMSE in Figure 1. If the uncertainty of the column $\beta_A^{299}$ measurements is estimated to be 20% which is

189    primarily due to the uncertainty of the $S$ *a priori* (a systematic error), we can estimate the corresponding uncertainty

190    for $\text{å}_\beta = 1.34$ to be $\pm 0.11$ by error propagation from Eq. (1). $\text{å}_\beta$ has important applications in aerosol type classification

191    from (spectral) aerosol lidar measurements (e.g., Cattrall et al., 2005; Hair et al., 2008; Müller et al., 2007). There is

192    significant variation in $\text{å}_\beta$ for 532–1064 nm reported in different studies, with numbers ranging from negative values

193    to 2.3 (Burton et al., 2012; Cattrall et al., 2005; Müller et al., 2007). However, all of these studies show a larger value

194    of $\text{å}_\beta$ for smoke and urban aerosols than for maritime and dust aerosols. Since most previous studies report $\text{å}_\beta$ for

195    wavelengths longer than 355 nm, $\text{å}_\beta$ calculated in this study for 299–532 nm could provide valuable data for UV

196    wavelengths.

197        In practice, aerosol extinction is a more meaningful parameter and more relevant for several applications than

198    backscatter. For the HSRL, the extinction coefficients are linearly converted from the backscatter coefficients by

199    assuming a constant $S = 55$ sr with 20% uncertainty, in the same manner as Reid et al. (2017). The estimated Ångström

200    exponent for 299 and 532 nm is $1.49 \pm 0.16$, using the data in Figure 1 after considering uncertainties in $S$ for both

201    lidars. The calculated Ångström exponent is different from the backscatter-related wavelength exponent because of

202    the wavelength dependence of $S$. The Ångström exponent from this study ($1.49 \pm 0.16$) is within a reasonable range

203    compared to previous studies. For example, the Ångström exponent was measured by a Raman lidar to be between

204    $1.35 \pm 0.2$ and $1.56 \pm 0.2$ at 355 nm for smoke aerosols in Canada (Strawbridge et al., 2018). The Ångström exponent

205    for urban aerosols was measured to be $1.4 \pm 0.5$ in Europe and $1.7 \pm 0.5$ in North America for 355 and 532 nm (Müller

206    et al., 2007).

207        The Aerosol Robotic Network (AERONET) (Holben et al., 1998) provides aerosol optical depth (AOD)

208    measurements in eight spectral bands between 340 and 1020 nm with a temporal resolution of about 15 min. The

209    measurement uncertainty for AERONET AOD is within 0.02 and is expected to be larger in the UV bands (Eck et al.,

210    1999; Holben et al., 2001). Even though the measurement is at a different wavelength, the AERONET AOD at 340

211    nm can provide an additional constraint for the choice of $S$ for the RO₃QET aerosol retrieval, especially since both

212    instruments are at the same location. Figure 2 presents the intercomparison of the RO₃QET lidar derived AOD at 299

213    nm and all available AOD data at 340 nm (Smirnov et al., 2000) from the collocated AERONET sun-sky radiometer

214    (data for 21–23 June is unavailable). The near surface region is assumed to be homogeneous and assigned the same

215    aerosol extinction values as the lowest available 30-m layer from the RO₃QET retrievals. Then, the aerosol extinction

216    coefficients are integrated from 0 to 6 km asl to calculate the lidar-derived AOD. The omission of aerosol extinction

217    above 6 km and the homogeneity assumption for the near surface region are sources of bias for the comparison since

218    the AERONET instrument measures the total column AOD. The lidar has more data and higher temporal resolution,

219    therefore, the lidar-derived AOD is interpolated to the AERONET measurement times. Figure 2 shows that the AOD

220    retrieved by the two instruments has a correlation coefficient of 0.97 and a small RMSE for a total duration of about

221 31 hours. The mean percentage difference between the RO$_3$QET and AERONET AOD is 15±9%. The *S a priori*

222 directly affects the AOD calculation. The lidar-derived AOD is on average 15% larger than the AERONET AOD due

223 to the shorter wavelength of the lidar measurement suggesting that the choice of $S = 60$ sr is appropriate. For a rough

224 estimation, the 1-σ standard deviation (9%) of the differences can be considered as the uncertainty of $S$ if the variability

225 of these differences are mostly due to the variation in $S$. Considering that AERONET measures the column average

226 AOD, with longer temporal integration, has its own uncertainty, and covers only 38% of the total observational period,

227 our assumption for $S = 60±20\%$ sr is appropriate for RO$_3$QET lidar profiling measurements with higher temporal and

228 vertical resolution and should be good enough to cover various uncertainty sources. The collocated AERONET data

229 enhances the credibility of our lidar aerosol retrieval and help evaluate the *S a priori*, with the caveat that the 124

230 paired data covering 31 hours is not a large sample. We do not show HSRL-AERONET comparison here since Reid

231 et al. (2017) has done so using more extensive data in a visible band taken at the UAH site in summer 2013.

232 Figure 3 presents the intercomparison of the aerosol backscatter retrieved by the HSRL and the RO$_3$QET

233 lidar for the four cases in 2013. The HSRL-derived aerosol backscatter coefficients are scaled to 299 nm (represented

234 by "HSRL-converted" hereafter) using the best-fit exponent value å$_\beta$=1.34. Some clouds lower than 2 km show up in

235 the HSRL curtains but not in the RO$_3$QET curtains (e. g., 1500–2100 on 15 August and 1500–2100 on 28 August).

236 These low-cloud-contaminated data were discarded in the RO$_3$QET lidar pre-processing program since the ozone lidar

237 probes the atmosphere with a shorter wavelength than the HSRL, and is therefore more affected by cloud interference.

238 Profiles with clouds higher than 2 km measured by the RO$_3$QET were retained and the aerosol retrievals below the

239 clouds were used for the range-resolving intercomparisons.

240 In terms of the aerosol measurement evaluation, we pay attention to the two capabilities of the RO$_3$QET lidar:

241 measuring the PBL diurnal evolution and measuring free-tropospheric smoke layers. In Figure 3, the PBL heights

242 measured by the two lidars, which are identified by large aerosol gradients, are highly consistent for all cases. The

243 development of the convective mixing layer in the early morning, an important process responsible for surface ozone

244 increase, can be visually identified in most RO$_3$QET curtains (e.g., 1400–1700 UTC or 0900–1200 local time in Figure

245 3-h). The aerosol structures and evolution in the free troposphere measured by the RO$_3$QET lidar are highly similar to

246 those measured by the HSRL. For example, the RO$_3$QET lidar captured an extremely thin aerosol layer at ~5-km

247 altitude on 27–28 August (Figure 3-g), which probably originated from the Pacific Northwest fire and has been

248 discussed by Reid et al. (2017). The large aerosol uncertainties for the RO$_3$QET lidar at far ranges are consistent with

249 expectation. As demonstrated in Appendix B, aerosol retrieval uncertainties due to lidar signal measurement error and

250 the boundary value chosen at the reference altitude, two of the most important sources of uncertainty, increase with

251 altitude and may exceed 100% at ~7 km.

252 To evaluate the range-resolving capability of the ozone lidar for aerosol retrieval, we intercompared the

253 aerosol backscatter coefficients, for all cases, from the two instruments with a 10-min temporal resolution and a 30-

254 m vertical resolution after filtering out cloud-contaminated data, as shown in Figure 4. The high correlation coefficient

255 of 0.95 suggests that the RO$_3$QET lidar can capture the aerosol variability with high spatio-temporal resolution. The

256 correlation coefficient (0.95) between the two high vertical resolution retrievals is slightly lower than that between the

257 RO$_3$QET and column-averaged HSRL retrievals (0.99, see Figure 1) due to less vertical average. The HSRL-converted

258  backscatter is calculated using å$_\beta$=1.34 and the regression equation in Figure 1. We expect the slope of the data in

259  Figure 4 to be very close to 1. However, the actual slope is 1.08, reflecting the fact that there is a large fraction of

260  points with small aerosol backscatter and larger residuals in clean air (low aerosol) regions. This is not surprising since

261  the HSRL has higher measurement precision than the RO$_3$QET lidar so that their relative differences in clean air

262  regions can be large.

263     Figure 5 presents the mean and 1-σ standard deviations of the relative differences between RO$_3$QET and

264  HSRL retrievals, (RO$_3$QET-HSRL)/HSRL, to be compared with the theoretical 1-σ error calculated as outlined in

265  Appendix B. The HSRL measurements are considered as the "true" values to be compared with the RO$_3$QET

266  measurements. Both the theoretical and actual 1-σ values generally increase with altitude. The actual differences

267  between RO$_3$QET and HSRL measurements are mostly within or of comparable order of magnitude to the theoretical

268  calculation of the RO$_3$QET measurement uncertainties. The structures of the theoretical uncertainties are consistent

269  with the actual differences at most altitudes, with few exceptions. For example, the large discrepancies (red lines

270  compared to blue lines in Figure 5) occurring at ~4.5 km in Figure 5 (c) and ~1.5 km in Figure 5 (d) are primarily

271  because of small number division effects for the extremely clean atmospheric layers (also see Figure 3). Aerosol

272  backscatter of clean air can be accurately measured by the HSRL, but may be beyond the measurement sensitivity of

273  RO$_3$QET.

274     In Figure 5, the RO$_3$QET-measured aerosols are generally higher than the HSRL-measured aerosols between

275  5 and 6 km so that the RO$_3$QET-HSRL differences are biased to positive altitude values. These positive biases can be

276  caused by two reasons. First, the RO$_3$QET derived aerosol extinction above 5 km is obviously larger than that from

277  HSRL during daytime due to the solar background impact, which is especially strong in the summer. The relative

278  differences are even worse in clean (compared to turbid) regions during the daytime because of the small number

279  division effect mentioned earlier. It can be seen from Figure 3 that RO$_3$QET nighttime retrievals above 5 km and

280  daytime retrievals below 5 km are relatively good due to either lower solar background or larger lidar signal resulting

281  in better SNR. There were both clean and smoky layers between 5 and 6 km for the four cases; therefore, the positive

282  differences cannot be explained solely by the lower capability of RO$_3$QET for measuring clean air. We hypothesize

283  that another reason causing the positive differences between 5 and 6 km is the underestimated backscatter color ratio

284  for the smoke aerosols. We converted the HSRL backscatter from 532 to 299 nm using a constant backscatter color

285  ratio, 1.34, which represents an average for the column-integrated backscatter. The most significant contribution to

286  integrated backscatter comes from PBL aerosols, which are mostly urban aerosols with a lower backscatter color ratio

287  than either fresh or aged smoke (Burton et al., 2012; Cattrall et al., 2005). The uncertainty of the backscatter color

288  ratio was not considered in the error budget of the aerosol retrieval. In addition, we ignored the measurement

289  uncertainty of the HSRL. Therefore, the general agreement oftheoretical estimates of aerosol retrieval uncertainties

290  and the actual errors suggests that our analysis of the uncertainty sources in Appendix B is reasonable.

291  **4. Conclusions**

292  We have evaluated the aerosol retrievals at 299 nm from the RO$_3$QET ozone lidar using both aerosol retrievals at 532

293  nm from the University of Wisconsin HSRL and AERONET AOD data at 340 nm from coincident observations at

294  Huntsville, AL in 2013. The integrated backscatter coefficients below 6 km asl from RO$_3$QET and HSRL are highly

correlated, with a Pearson coefficient of 0.99 after excluding cloud-contaminated data. The aerosol profiles of backscatter coefficients at 30-m vertical and 10-min temporal resolution retrieved by RO₃QET are also highly correlated with those from the HSRL with a coefficient of 0.95 suggesting that the ozone lidar is capable of providing reliable aerosol structure information at high spatio-temporal resolution. Intercomparison of the backscatter product was performed to avoid additional uncertainty caused by the lidar ratio ($S$) assumption needed for the HSRL aerosol extinction retrieval. The RO₃QET-measured AOD below 6 km asl is also highly correlated with the AERONET-measured AOD, with a correlation coefficient of 0.97. The 340-nm band of the AERONET AOD data is closest to the ozone lidar wavelength among the available instruments and can therefore provide a constraint for the $S$ assumption for the ozone lidar. Analysis of the intercomparison of AERONET and RO₃QET data confirms that our choice of $S$ = 60 sr at 299 nm is appropriate.        The aerosol retrieval algorithm and its error budget are shown in the Appendix. The primary uncertainty sources for the aerosol lidar retrieval are errors in lidar signal measurement, boundary value assumption, air density calculation, $S$ *a priori*, and ozone profile input. The uncertainty in $S$ assumption is a dominant source at near range while the lidar signal measurement and boundary value errors dominate at far range, as shown in Figure B1 for a sample scenario. Within the middle range (PBL top – about 7 km), the air density calculation error is essential and is larger or comparable to the lidar signal measurement error. The total uncertainty generally increases with altitude from about 15% in the PBL to consistently higher than 100% above 7 km. Theoretical estimates of the error budget are generally consistent with RO₃QET-HSRL measurement differences.

By assuming a constant $S$ of 60 sr at 299 nm, the backscatter coefficients measured by RO₃QET and HSRL are related by a backscatter color ratio (backscatter-related exponent) of 1.34±0.11 for 299 and 532 nm. The extinction-related Ångström exponent, that is more relevant for various applications, is estimated to be 1.49±0.16 by assuming $S$ = 55 sr for the HSRL at 532 nm. These exponents represent a summertime average for a mixture of urban pollution and fire smoke. Separation of aerosol types was not done in this work, although we recognize that $S$ and Ångström exponent vary with the aerosol phase function and size distribution. Aerosol correction for ozone lidar retrievals will be described in a subsequent paper.

**Appendix A. Aerosol retrieval algorithm**

The ozone DIAL solution can be written as follows:

$$n_{(r)} = \frac{-1}{2\Delta\sigma} \times \frac{d}{dr}\left[ln\frac{P_{\text{on}(r)}}{P_{\text{off}(r)}}\right] + [B] + [E] \, , \tag{A1}$$

where $n_{(r)}$ is the ozone number density at range $r$, $\Delta\sigma$ is the differential ozone absorption cross section, $P_{\text{on}(r)}$ and $P_{\text{off}(r)}$ are the backscattered on-line and off-line lidar returns, and $[B]$ and $[E]$ represent the differential backscatter and extinction terms (Browell et al., 1985), respectively, including both molecular and aerosol components. The first term of the right side of Eq. (A1) is often called the signal term. The subscripts "on" and "off" represent 289 and 299 nm in this study. The aerosol extinction coefficients at 299 nm are calculated using the following procedure.

1)        A first-order Savitzky-Golay differentiation filter with a second-degree polynomial and variable fitting window widths are applied on $ln\frac{P_{\text{on}(r)}}{P_{\text{off}(r)}}$ to compute the signal term. This smoothing method can accommodate the

330 rapid decay of the lidar signal with altitude to provide sufficient SNR for ozone retrievals by appropriate selection of
331 smoothing window widths (Leblanc et al., 2016a).

332 2)  By canceling the lidar constant using the two lidar equations at range $r$ and $r+\Delta r$ for 299 nm, the aerosol
333 backscatter coefficients at range $r$ can be expressed as (Uchino et al., 1980):

334 $$\beta_A(r) = -\beta_M(r) + \frac{Z(r)}{Z(r+\Delta r)}[\beta_A(r+\Delta r) + \beta_M(r+\Delta r)]\exp\left\{-2\Delta r[\alpha_A\left(r+\frac{\Delta r}{2}\right) + \alpha_M\left(r+\frac{\Delta r}{2}\right) + \alpha_{O3}\left(r+\frac{\Delta r}{2}\right)]\right\}$$ ,

335 (A2)

336 where $\beta_A(r)$ and $\beta_M(r)$ are aerosol and molecular backscatter coefficients at range $r$, respectively; $Z(r) = P_{off}r^2$ is
337 the range-corrected lidar signal at 299 nm; $\alpha_A(r+\Delta r/2)$, $\alpha_M(r+\Delta r/2)$, and $\alpha_{O3}(r+\Delta r/2)$ represent the average aerosol,
338 molecular, and ozone extinction coefficients between range $r$ and $r+\Delta r$, respectively. Assuming the 299-nm lidar ratio,
339 $S=\alpha_A/\beta_A$, is constant with the range at 60 sr for this study and further assuming:

340 $$\alpha_A(r+\frac{\Delta r}{2}) \approx \alpha_A(r+\Delta r) = S\beta_A(r+\Delta r),$$  (A3)

341 Eq. (A2) contains only two unknown variables: the aerosol backscatter coefficient $\beta_A(r+\Delta r)$ and ozone extinction
342 coefficient $\alpha_{O3}(r+\Delta r/2)$, which requires knowledge of the ozone number density $n_{(r+\Delta r/2)}$. Molecular backscatter and
343 extinction can be computed from nearby radiosonde data or a model with acceptable accuracy. For the first iteration
344 step, $n_{(r+\Delta r/2)}$ can be computed from the signal term in Eq. (A1). By assuming a start value $\beta_A(ref)$ at a reference
345 range and a constant $S$ with range, $\beta_A(r)$ can be solved by Equation (A2). Then, the first $\beta_A(r)$ profile is substituted
346 back into (A2) to compute the second estimate by using a more accurate form for $\alpha_A(r+\Delta r/2)$ as:

347 $$\alpha_A\left(r+\frac{\Delta r}{2}\right) = S[\beta_A(r+\Delta r) + \beta'_A(r)]/2,$$  (A4)

348 where $\beta'_A(r)$ represents the value from the first estimate. Typically, a stable solution for $\beta_A(r)$, which does not change
349 significantly from one iteration step to the next, can be obtained with only three iterations of Eq. (A2) and (A4.

350 3)  The correction terms, [B] and [E], in Eq. (A1) are calculated by the Browell et al. (1985) approximation,
351 assuming a power law dependence with wavelength for the aerosol extinction and choosing an appropriate Ångström
352 exponent. Since this paper focuses only on aerosol retrievals, the details of the ozone corrections will be described in
353 a future article.

354 4)  Aerosol profiles computed for the three altitude channels are finally merged to a single profile in their
355 overlapping altitude zones, 0.5–1 km for Channels-1 and 2, 1.5–2 km for Channels-2 and 3.

356

357 **Appendix B. Error budget of the aerosol retrieval**

358 Now we investigate five primary error sources affecting each term on the right side of Eq. (A2). In the following
359 section, we use the notation $\Delta$ to represent the absolute uncertainty and $\delta$ to represent the relative uncertainty. For a
360 function $Y$, derived from several measurement variables $x_1$, $x_2$, …, the uncertainty in $Y$ can be estimated by the
361 following expression using the first-order Taylor expansion approximation when these variables are independent
362 (Taylor, 1997):

363 $$\Delta Y^2 = (\Delta x_1 \frac{\partial Y}{\partial x_1})^2 + (\Delta x_2 \frac{\partial Y}{\partial x_2})^2 + \cdots .$$  (B1)

364 **B.1 Lidar signal measurement error**

365  The error source to determine the normalized lidar signal ratio term $\frac{Z(r)}{Z(r+\Delta r)}$ is the lidar signal measurement error, $\Delta P$.

366  Although $\Delta P$ may be due to various processes such as inaccurate dead-time correction, inaccurate background

367  subtraction, and signal-induced noise, its dominant component is the lidar signal statistical uncertainty (often called

368  lidar signal detection noise) and is typically assumed to obey a Poisson distribution. Assuming no error in deciding $r$,

369  by using Eq. (A2) and (B1) we obtain the uncertainty of the aerosol backscatter owing to lidar signal measurement

370  error, $\Delta\beta_A^{sig}(r)$, relative to the total backscatter as:

$$371 \qquad \frac{\Delta\beta_A^{sig}(r)}{\beta_A(r)+\beta_M(r)} = \sqrt{[\delta P(r)]^2 + [\delta P(r+\Delta r)]^2}, \qquad (B2)$$

372  where $P(r)$ represents lidar signal counts at $r$ after omitting the wavelength subscript (i.e., 299 nm) and $\delta P(r)$ is just

373  the inverse of SNR. This means that the uncertainty of the aerosol backscatter coefficient due to lidar signal

374  measurement is determined by the lidar SNR similarly to other remote sensing detection techniques. Consequently,

375  its relative uncertainty can be written as:

$$376 \qquad \delta\beta_A^{sig}(r) = \left(\frac{1}{B(r)}+1\right)\sqrt{[\delta P(r)]^2 + [\delta P(r+\Delta r)]^2}, \qquad (B3)$$

377  where $B(r)= \beta_A(r)/\beta_M(r)$ is the aerosol-to-molecular backscatter ratio. As expected, $\delta\beta_A^{sig}(r)$ has a reverse relationship

378  with $\beta_A(r)$ since it is a relative uncertainty. Figure B1 shows an example of the uncertainty budget for a 10-min lidar

379  data profile. The aerosol retrieval uncertainty due to the lidar signal measurement error generally increases with

380  altitude primarily because of the rapidly decaying lidar SNR.

381  **B.2 Boundary value error**

382  According to Eq. (A2), the uncertainty of the aerosol backscatter at $r$, $\beta_A(r)$ , can be induced by the uncertainty of the

383  backscatter at $r + \Delta r$, $\beta_A(r + \Delta r)$, due to the iterative computation method. The error propagation between the

384  adjacent altitudes can be determined by their partial differential relationship. Using the traditional far-end solution by

385  assuming that the air is clean at a reference altitude, the aerosol uncertainty due to the inaccurate boundary value

386  assumption propagates downward based on the following equation:

$$387 \qquad \delta\beta_A^{BV}(r) = \delta\beta_A(r + \Delta r)\left[\frac{1+\frac{1}{B(r)}}{1+\frac{1}{B(r+\Delta r)}}\right]\{1 - 2S\Delta r\beta_A(r + \Delta r)[1 + \frac{1}{B(r+\Delta r)}]\}. \qquad (B4)$$

388  The yellow line in Figure B1 represents the relative uncertainty of backscatter retrieval due to the boundary value

389  assumption, $\delta\beta_A^{BV}(r)$, when $\delta\beta_A(r_b) = 1000\%$ (i.e., 10 times overestimate at $r_b$ =10 km). Despite a large

390  overestimate at the reference altitude, $\delta\beta_A^{BV}(r)$ decreases toward the ground, to less than 10% below 5.5 km and less

391  than 1% below 3.5 km. Simulations demonstrate that $\delta\beta_A^{BV}(r)$ for an underestimation of $\delta\beta_A(r_b)$ (not shown) is better

392  than that for an overestimation, indicating that the boundary value is preferred at a smaller value. As suggested by Eq.

393  (B4), $\delta\beta_A^{BV}(r)$ is affected by both $S$ and $B$. Larger $S$ (if it is correct) results in smaller $\delta\beta_A^{BV}(r)$ and, therefore, aerosol

394  retrieval errors converge to zero faster. In other words, the smaller the value of $S$ is, the more sensitive the aerosol

395  retrieval is to the boundary value error. $\delta\beta_A^{BV}(r)$ decreases with an increase of $B(r)$. This means that $\delta\beta_A^{BV}(r)$ is less

396  affected by the assumed value of $\beta_A(r_b)$ when the aerosol backscatter becomes more important relative to molecular

397  backscatter, which occurs at longer wavelengths or under turbid air conditions. It is to be noted that $\delta\beta_A(r_b)$ is

398  between -1 and $+\infty$ so that the distribution of $\delta\beta_A^{BV}(r)$ is asymmetric with the zero axis.

399    In terms of the influence of the boundary value error, we have compared our calculation with an analytical

400    solution proposed by Kovalev and Moosmüller (1994) (not shown); the results are almost identical. Aerosol retrieval

401    uncertainty due to incorrect boundary value assumption tends to converge to zero towards the lidar. It is negligible at

402    lower altitudes, especially in the PBL, when the air is turbid.

403    **B.3 Air density error**

404    According to Eq. (A2), the air density profile affects $\beta_M(r)$, $\beta_M(r+\Delta r)$, and the optical depth (or transmittance).

405    Similarly, we can derive the relative uncertainty in aerosol backscatter owing to the uncertainty in the air density

406    profile as:

407    $\delta \beta_A^{AD}(r)$

408    $$= \sqrt{\left\{\frac{\delta\beta_M(r)}{B(r)}\left[1 + S_m\Delta r\beta_A(r) + S_m\Delta r\beta_M(r)\right]\right\}^2 + \left\{\frac{\delta\beta_M(r+\Delta r)\left[\frac{1}{B(r)}+1\right]}{B(r+\Delta r)+1}\left[1 - S_m\Delta r\beta_A(r+\Delta r) - S_m\Delta r\beta_M(r+\Delta r)\right]\right\}^2}$$

409    . (B5)

410    $S_m$ represents the molecular extinction-to-backscatter ratio, which is a constant ($8\pi/3$). The two parts in the square root

411    are the components due to the uncertainties at $r$ and $r+\Delta r$, respectively. Each component includes the influences from

412    both molecular backscatter and optical depth. When $\Delta r$ is small, the contribution of the optical depth error is much

413    smaller than that of the molecular backscatter error so that (B4) can be approximated as:

414    $$\delta\beta_A^{AD}(r) \approx \sqrt{2}\frac{\delta\beta_M(r)}{B(r)}. \tag{B6}$$

415    It is to be noted that $\Delta\beta_M(r)$ and $\Delta\beta_M(r+\Delta r)$ are independent errors as assumed in Eq. (B1). If they are correlated, Eq.

416    (B5) will partly cancel out with their covariance term, which is not shown in (B1). Due to the nature of the iterative

417    computation method, $\delta\beta_A^{AD}(r + \Delta r)$ affects $\delta\beta_A^{AD}(r)$ as noted in Eq. (B4), so that the aerosol retrieval uncertainty due

418    to air density error will propagate downward. However, model simulation suggests that the systematic error of the air

419    density calculation has little impact on the aerosol retrieval because of the cancelation of the effect at $r$ and $r + \Delta r$. Eq.

420    (B6) means the uncertainty in the calculation of molecular backscatter will mostly linearly propagate to aerosol

421    backscatter. If the 2-$\sigma$ precision of a radiosonde is 0.3 K and 0.5 hPa for temperature and pressure measurements

422    (Hurst et al., 2011), the propagated uncertainty onto molecular backscatter is only about 0.1%. However, the real

423    disturbance of an atmosphere deviating from the actual air density profile may be more significant since there are

424    usually only a few radiosonde profiles available every day. Hence, we assume $\delta\beta_M(r)$ to be 1% and the resulting

425    aerosol retrieval uncertainty is represented by the green line in Figure B1. $\delta\beta_A^{AD}(r)$ can be tens of percent in the free

426    troposphere and is an important error source for aerosol retrievals (Russell et al., 1979). $\delta\beta_A^{AD}(r)$ is less than 10% in

427    the PBL because of more turbid air in that region. Since $\delta\beta_M(r)$ is assumed to be a constant in this example, the

428    variation of $\delta\beta_A^{AD}(r)$ is mostly a result of varying $B(r)$, the aerosol-to-molecular backscatter ratio. Since $B(r)$ generally

429    increases with an increase in wavelength, $\delta\beta_A^{AD}(r)$ is expected to be smaller at longer wavelengths. Therefore, the

430    aerosol retrieval is less sensitive to the air density error at longer wavelengths.

431    **B.4 Lidar ratio error**

432    By using Eqn. (A2) and (B1), the relative uncertainty in aerosol backscatter due to incorrect lidar ratio ($S$) assumption

433    can be calculated as follows:

434
$$\delta\beta_A^S(r) = 2\left[\frac{1}{B(r)} + 1\right]\Delta S\beta_A(r)\Delta r. \tag{B7}$$

435  $\delta\beta_A^S(r)$ due to $\Delta S$ at only range $r$ appears to be small, about 1%, when $\Delta r$ is specified at 22.5 m. However, $\Delta S$ varying

436  with altitude is mostly systematic and, therefore, $\delta\beta_A^S(r)$ at every altitude will propagate downward and these effects

437  will accumulate. The error accumulation is not straightforward to compute as an analytical solution. However, these

438  effects can be simulated numerically. $S$ is highly variable and it is difficult to estimate its actual uncertainty range. In

439  this study, we assume that $\delta S = 20\%$ (or $\Delta S$ =12 sr) according to both previous study (Müller et al., 2007) and the

440  analysis using the collocated AERONET AOD data at 340 nm. The light-blue line in Figure B1 shows that the

441  accumulative uncertainties in the aerosol backscatter due to $\Delta S$ using Eq. (B7) and (B4) are close to the assumed 20%

442  uncertainty for $\delta S$. $\delta\beta_A^S(r)$ is the largest error source in the PBL which is the near range of the lidar. $\delta\beta_A^S(r)$ decreases

443  with an increase in wavelength because of increasing $B(r)$. In other words, $\delta\beta_A^S(r)$ is less sensitive to $\Delta S$ at longer

444  wavelengths.

445  **B.5 Ozone error**

446  Similar to $S$, the ozone uncertainty affects only the transmittance term in Eqn. (A2) and its error propagation on aerosol

447  backscatter retrieval can be expressed as:

448
$$\delta\beta_A^{O3}(r) = 2\left[\frac{1}{B(r)} + 1\right]\Delta\alpha_{O3}(r)\Delta r. \tag{B8}$$

449  $\delta\beta_A^{O3}(r)$ is proportional to the $\left[\frac{1}{B(r)} + 1\right]$ factor and ozone absorption uncertainty, meaning that $\delta\beta_A^{O3}(r)$ is smaller at

450  longer wavelengths due to larger aerosol scattering ratio and smaller ozone absorption. When $\Delta r$ is specified at 22.5

451  m, $\delta\beta_A^{O3}(r)$ is less than 0.3%. We still simulate the vertical accumulation of $\delta\beta_A^{O3}(r)$ using Eq. (B4). As noted earlier,

452  the systematic errors of the DIAL ozone measurement tend to accumulate while the random errors tend to cancel out.

453  The dominant error source for lidar measurements at the far range is typically the lidar signal detection noise, a type

454  of random error. Therefore, for purposes of estimation, we assume a 5% constant DIAL retrieval uncertainty primarily

455  covering the uncertainties due to ozone absorption cross section, non-ozone gas interference, and signal saturation

456  effect (Leblanc et al., 2018; Wang et al., 2017). As shown in Figure B1, the simulated aerosol retrieval uncertainty

457  due to ozone is relatively minor and is less than 5% at most altitudes.

458  In summary, the uncertainties in aerosol backscatter retrieval for the ozone lidar are controlled by $\Delta S$ at near

459  ranges (i. e., in the PBL) where the air is most turbid and are determined by both the lidar signal detection error and

460  inaccurate boundary value assumption at far ranges (higher than 7 km) where the air is typically clear. In the middle

461  range of the lidar measurement (PBL top – 7 km), the air density calculation error may become a significant error

462  source for aerosol retrieval and may have a comparable influence on the aerosol retrieval as the lidar signal

463  measurement error. Relative to the above four uncertainty sources, ozone DIAL retrieval error is relatively

464  unimportant especially in the lower altitudes where lidar SNR is large enough. All the uncertainty terms are affected

465  by the aerosol-to-molecular backscatter ratio, $B(r)$, which represents the relative importance of the aerosol component

466  in both extinction and backscatter processes. Based on the above uncertainty budget analysis, we conclude that the

467  RO$_3$QET lidar is capable of measuring aerosol profile reliably below 6 km with the current laser output power.

468

469  **Acknowledgements**

470  The authors thank the National Aeronautics and Space Administration (NASA)'s Science Mission Directorate for
471  supporting the TOLNet program. A portion of the research was carried out at the Jet Propulsion Laboratory, California
472  Institute of Technology, under a contract with the National Aeronautics and Space Administration
473  (80NM0018D0004). The views, opinions, and findings contained in this report are those of the authors and should not
474  be construed as an official NASA, National Oceanic and Atmospheric Administration, or U.S. Government position,
475  policy, or decision.

476

477  **References**

478  Ackermann, J. (1998). The extinction-to-backscatter ratio of tropospheric aerosol: A numerical study. *Journal of*
479       *atmospheric and oceanic technology*, *15*(4), 1043-1050.
480  Alvarez, R. J., Senff, C. J., Langford, A. O., Weickmann, A. M., Law, D. C., Machol, J. L., ... & Hardesty, R. M.
481       (2011). Development and application of a compact, tunable, solid-state airborne ozone lidar system for
482       boundary layer profiling. *Journal of Atmospheric and Oceanic Technology*, *28*(10), 1258-1272.
483  Ångström, A. (1929). On the atmospheric transmission of sun radiation and on dust in the air. *Geografiska Annaler*,
484       *11*(2), 156-166.
485  Browell, E. V., Ismail, S., and Shipley, S. T. (1985). Ultraviolet DIAL measurements of O3 profiles in regions of
486       spatially inhomogeneous aerosols, Appl. Opt., 24(17), 2827-2836.
487  Browell, E. V., Fenn, M. A., Butler, C. F., Grant, W. B., Harriss, R. C., & Shipham, M. C. (1994). Ozone and aerosol
488       distributions in the summertime troposphere over Canada. *Journal of Geophysical Research: Atmospheres*,
489       *99*(D1), 1739-1755.
490  Burton, S. P., Ferrare, R. A., Hostetler, C. A., Hair, J. W., Rogers, R. R., Obland, M. D., ... & Froyd, K. D. (2012).
491       Aerosol classification using airborne High Spectral Resolution Lidar measurements–methodology and
492       examples. *Atmospheric Measurement Techniques*, *5*(1), 73-98.
493  Cattrall, C., Reagan, J., Thome, K., & Dubovik, O. (2005). Variability of aerosol and spectral lidar and backscatter
494       and extinction ratios of key aerosol types derived from selected Aerosol Robotic Network locations. *Journal*
495       *of Geophysical Research: Atmospheres*, *110*(D10).
496  De Young, R., Carrion, W., Ganoe, R., Pliutau, D., Gronoff, G., Berkoff, T., & Kuang, S. (2017). Langley mobile
497       ozone lidar: ozone and aerosol atmospheric profiling for air quality research. *Applied optics*, *56*(3), 721-730.
498  Eck, T. F., Holben, B. N., Reid, J. S., Dubovik, O., Smirnov, A., O'neill, N. T., ... & Kinne, S. (1999). Wavelength
499       dependence of the optical depth of biomass burning, urban, and desert dust aerosols. *Journal of Geophysical*
500       *Research: Atmospheres*, *104*(D24), 31333-31349.
501  Eisele, H., & Trickl, T. (2005). Improvements of the aerosol algorithm in ozone lidar data processing by use of
502       evolutionary strategies. *Applied optics*, *44*(13), 2638-2651.
503  Eloranta, E. E. (2005). High spectral resolution lidar. In *Lidar* (pp. 143-163). Springer, New York, NY.
504  Fernald, F. G. (1984). Analysis of atmospheric lidar observations: some comments. *Applied optics*, *23*(5), 652-653.

Fukuchi, T., Fujii, T., Cao, N., Nemoto, K., & Takeuchi, N. (2001). Tropospheric O3 measurement by simultaneous differential absorption lidar and null profiling and comparison with sonde measurement. *Optical Engineering*, *40*.

Gronoff, G., Robinson, J., Berkoff, T., Swap, R., Farris, B., Schroeder, J., ... & Adcock, E. E. (2019). A method for quantifying near range point source induced O3 titration events using Co-located Lidar and Pandora measurements. *Atmospheric Environment*, *204*, 43-52.

Grund, C. J., & Eloranta, E. W. (1991). University of Wisconsin high spectral resolution lidar. *Optical Engineering*, *30*(1), 6-13.

Groß, S., Esselborn, M., Weinzierl, B., Wirth, M., Fix, A., & Petzold, A. (2013). Aerosol classification by airborne high spectral resolution lidar observations. *Atmospheric chemistry and physics*, *13*(5), 2487-2505.

Hair, J. W., Hostetler, C. A., Cook, A. L., Harper, D. B., Ferrare, R. A., Mack, T. L., ... & Hovis, F. E. (2008). Airborne high spectral resolution lidar for profiling aerosol optical properties. *Applied optics*, *47*(36), 6734-6752.

Holben, B. N., Eck, T. F., Slutsker, I. A., Tanre, D., Buis, J. P., Setzer, A., ... & Lavenu, F. (1998). AERONET—A federated instrument network and data archive for aerosol characterization. *Remote sensing of environment*, *66*(1), 1-16.

Holben, B. N., Tanre, D., Smirnov, A., Eck, T. F., Slutsker, I., Abuhassan, N., ... & Kaufman, Y. J. (2001). An emerging ground-based aerosol climatology: Aerosol optical depth from AERONET. *Journal of Geophysical Research: Atmospheres*, *106*(D11), 12067-12097.

Hurst, D. F., Hall, E. G., Jordan, A. F., Miloshevich, L. M., Whiteman, D. N., Leblanc, T., ... & Oltmans, S. J. (2011). Comparisons of temperature, pressure and humidity measurements by balloon-borne radiosondes and frost point hygrometers during MOHAVE-2009. *Atmospheric Measurement Techniques*, *4*(12), 2777-2793.

Immler, F. (2003). A new algorithm for simultaneous ozone and aerosol retrieval from tropospheric DIAL measurements. *Applied Physics B*, *76*(5), 593-596.

Kempfer, U., Carnuth, W., Lotz, R., & Trickl, T. (1994). A wide-range ultraviolet lidar system for tropospheric ozone measurements: Development and application. *Review of scientific instruments*, *65*(10), 3145-3164.

Klein, A., Ravetta, F., Thomas, J. L., Ancellet, G., Augustin, P., Wilson, R., ... & Pelon, J. (2019). Influence of vertical mixing and nighttime transport on surface ozone variability in the morning in Paris and the surrounding region. *Atmospheric environment*, *197*, 92-102.

Klett, J. D. (1981). Stable analytical inversion solution for processing lidar returns. *Applied optics*, *20*(2), 211-220.

Klett, James D. "Lidar inversion with variable backscatter/extinction ratios." *Applied optics* 24.11 (1985): 1638-1643.

Kovalev, V. A., & Eichinger, W. E. (2004). *Elastic lidar: theory, practice, and analysis methods*. John Wiley & Sons.

Kovalev, V. A., & Moosmüller, H. (1994). Distortion of particulate extinction profiles measured with lidar in a two-component atmosphere. *Applied optics*, *33*(27), 6499-6507.

Kovalev, V. A., & McElroy, J. L. (1994). Differential absorption lidar measurement of vertical ozone profiles in the troposphere that contains aerosol layers with strong backscattering gradients: a simplified version. *Applied optics*, *33*(36), 8393-8401.

541 Kuang, S., Burris, J. F., Newchurch, M. J., Johnson, S., and Long, S.: Differential Absorption Lidar to Measure
542     Subhourly Variation of Tropospheric Ozone Profiles, IEEE Transactions on Geoscience and Remote Sensing,
543     49, 557-571, 10.1109/TGRS.2010.2054834, 2011.

544 Kuang, S., Newchurch, M. J., Burris, J., and Liu, X.: Ground-based lidar for atmospheric boundary layer ozone
545     measurements, Appl. Opt., 52, 3557-3566, 10.1364/AO.52.003557, 2013.

546 Kuang, S., Newchurch, M. J., Johnson, M. S., Wang, L., Burris, J., Pierce, R. B., ... & Warneke, C. (2017).
547     Summertime tropospheric ozone enhancement associated with a cold front passage due to stratosphere-to-
548     troposphere transport and biomass burning: Simultaneous ground-based lidar and airborne measurements.
549     *Journal of Geophysical Research: Atmospheres*, *122*(2), 1293-1311.

550 Langford, A. O., Alvarez, I. I., Raul, J., Kirgis, G., Senff, C. J., Caputi, D., ... & McNamara, M. E. (2019).
551     Intercomparison of lidar, aircraft, and surface ozone measurements in the San Joaquin Valley during the
552     California Baseline Ozone Transport Study (CABOTS). *Atmospheric Measurement Techniques*, *12*(3), 1889-
553     1904.

554 Langford, A. O., Alvarez, R. J., Brioude, J., Caputi, D., Conley, S. A., Evan, S., ... & Ryoo, J. M. (2020). Ozone
555     production in the Soberanes smoke haze: implications for air quality in the San Joaquin Valley during the
556     California Baseline Ozone Transport Study. *Journal of Geophysical Research: Atmospheres*, *125*(11),
557     e2019JD031777.

558 Leblanc, T., Sica, R. J., van Gijsel, J. A. E., Godin-Beekmann, S., Haefele, A., Trickl, T., Payen, G., and Gabarrot, F.:
559     Proposed standardized definitions for vertical resolution and uncertainty in the NDACC lidar ozone and
560     temperature algorithms – Part 1: Vertical resolution, Atmos. Meas. Tech., 9, 4029-4049, 10.5194/amt-9-
561     4029-2016, 2016a.

562 Leblanc, T., Sica, R.J., Van Gijsel, J.A., Godin-Beekmann, S., Haefele, A., Trickl, T., Payen, G. and Liberti, G., 2016.
563     Proposed standardized definitions for vertical resolution and uncertainty in the NDACC lidar ozone and
564     temperature algorithms–Part 2: Ozone DIAL uncertainty budget. Atmospheric Measurement Techniques,
565     9(8), pp.4051-4078, 2016b.

566 Leblanc, T., Brewer, M. A., Wang, P. S., & Granados Muñoz, M. J. (2018). Validation of the TOLNet lidars: the
567     Southern California Ozone Observation Project (SCOOP). *Atmospheric measurement techniques*, *11*, 6137-
568     6162.

569 McDermid, I. S., Beyerle, G., Haner, D. A., & Leblanc, T. (2002). Redesign and improved performance of the
570     tropospheric ozone lidar at the Jet Propulsion Laboratory Table Mountain Facility. *Applied optics*, *41*(36),
571     7550-7555.

572 Mishchenko, M. I., Travis, L. D., Kahn, R. A., & West, R. A. (1997). Modeling phase functions for dustlike
573     tropospheric aerosols using a shape mixture of randomly oriented polydisperse spheroids. *Journal of
574     Geophysical Research: Atmospheres*, *102*(D14), 16831-16847.

575 Müller, D., Ansmann, A., Mattis, I., Tesche, M., Wandinger, U., Althausen, D., & Pisani, G. (2007). Aerosol-type-
576     dependent lidar ratios observed with Raman lidar. *Journal of Geophysical Research: Atmospheres*,
577     *112*(D16).

578    Newell, R. E., Thouret, V., Cho, J. Y., Stoller, P., Marenco, A., & Smit, H. G. (1999). Ubiquity of quasi-horizontal
579            layers in the troposphere. *Nature*, *398*(6725), 316.

580    Papayannis, A. D., Porteneuve, J., Balis, D., Zerefos, C., & Galani, E. (1999). Design of a new DIAL system for
581            tropospheric and lower stratospheric ozone monitoring in Northern Greece. *Physics and Chemistry of the*
582            *Earth, Part C: Solar, Terrestrial & Planetary Science*, *24*(5), 439-442.

583    Proffitt, M. H., & Langford, A. O. (1997). Ground-based differential absorption lidar system for day or night
584            measurements of ozone throughout the free troposphere. *Applied optics*, *36*(12), 2568-2585.

585    Reid, J. S., Kuehn, R. E., Holz, R. E., Eloranta, E. W., Kaku, K. C., Kuang, S., ... & Atwood, S. A. (2017). Ground-
586            based High Spectral Resolution Lidar observation of aerosol vertical distribution in the summertime
587            Southeast United States. *Journal of Geophysical Research: Atmospheres*, *122*(5), 2970-3004.

588    Russell, P. B., Swissler, T. J., & McCormick, M. P. (1979). Methodology for error analysis and simulation of lidar
589            aerosol measurements. *Applied Optics*, *18*(22), 3783-3797.

590    Smirnov, A., Holben, B. N., Eck, T. F., Dubovik, O., & Slutsker, I. (2000). Cloud-screening and quality control
591            algorithms for the AERONET database. *Remote sensing of environment*, *73*(3), 337-349.

592    Steinbrecht, W., & Carswell, A. I. (1995). Evaluation of the effects of Mount Pinatubo aerosol on differential
593            absorption lidar measurements of stratospheric ozone. *Journal of Geophysical Research: Atmospheres*,
594            *100*(D1), 1215-1233.

595    Strawbridge, K. B., Travis, M. S., Firanski, B. J., Brook, J. R., Staebler, R., & Leblanc, T. (2018). A fully autonomous
596            ozone, aerosol and nighttime water vapor lidar: a synergistic approach to profiling the atmosphere in the
597            Canadian oil sands region. *Atmospheric Measurement Techniques*, *11*(12), 6735-6759.

598    Sullivan, J. T., McGee, T. J., Sumnicht, G. K., Twigg, L. W., & Hoff, R. M. (2014). A mobile differential absorption
599            lidar to measure sub-hourly fluctuation of tropospheric ozone profiles in the Baltimore–Washington, DC
600            region. *Atmospheric Measurement Techniques*, *7*(10), 3529-3548.

601    Taylor, J. (1997). *Introduction to error analysis, the study of uncertainties in physical measurements*.

602    Uchino, O., Maeda, M., Shibata, T., Hirono, M., & Fujiwara, M. (1980). Measurement of stratospheric vertical ozone
603            distribution with a Xe–Cl lidar; estimated influence of aerosols. *Applied optics*, *19*(24), 4175-4181.

604    Uchino, O., & Tabata, I. (1991). Mobile lidar for simultaneous measurements of ozone, aerosols, and temperature in
605            the stratosphere. *Applied optics*, *30*(15), 2005-2012.

606    Wang, L., Newchurch, M. J., Alvarez II, R. J., Berkoff, T. A., Brown, S. S., Carrion, W., DeYoung R. J., Johnson, B.
607            J., Ganoe, R., Gronoff, G., Kirgis G., Kuang, S., Langford, A. O., Leblanc T., McDuffie E. E., McGee, T. J.,
608            Pliutau, D., Senff, C. J., Sullivan, J. T., Sumnicht, G., Twigg, L. W., & Weinheimer, A. J. (2017). Quantifying
609            TOLNet ozone lidar accuracy during the 2014 DISCOVER-AQ and FRAPPE campaigns. *Atmospheric*
610            *Measurement Techniques*, 10(10), 3865-3876.

611
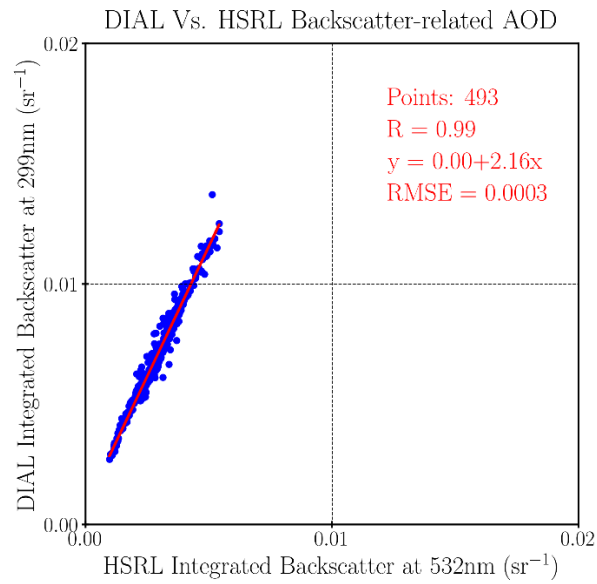
612

613 Figure 1. Regression of ozone DIAL and HSRL derived integrated aerosol backscatter between 0.4 and 6 km asl using

614 the best least-squares fit, resulting in a backscatter color ratio of 1.34 for 299–532-nm for four cases in 2013. All the

615 data was taken at Huntsville, AL, USA, during summer 2013.

616
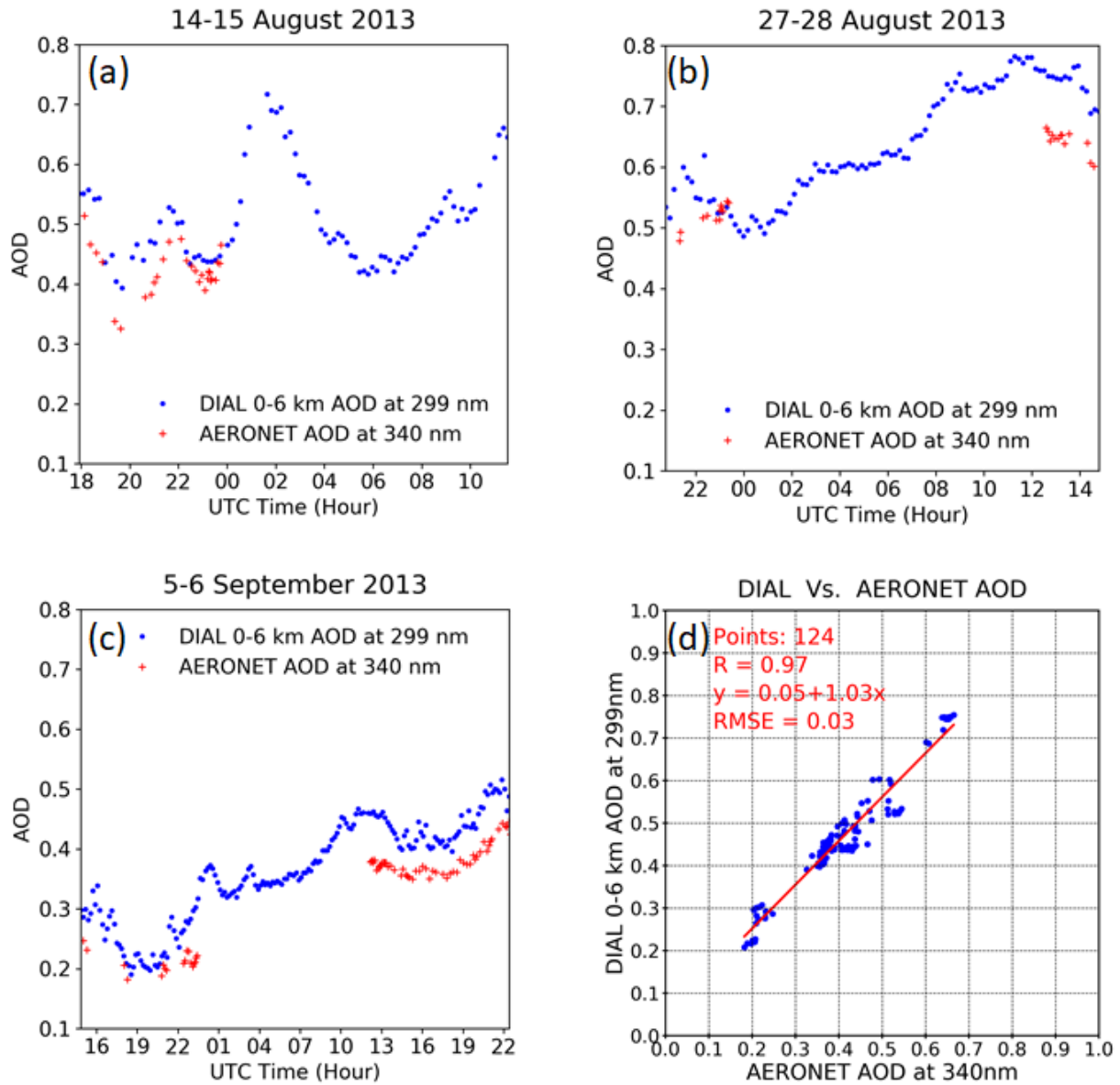
Figure 2. RO₃QET DIAL derived AOD between 0 and 6 km at 299 nm using *S*=60 sr compared to collocated
AERONET AOD at 340 nm for (a) 14–15 August, (b) 27–28 August, and (c) 5–6 September, 2013. (d) Regression of
the paired data after the DIAL AOD is interpolated to the times of AERONET AOD measurements.
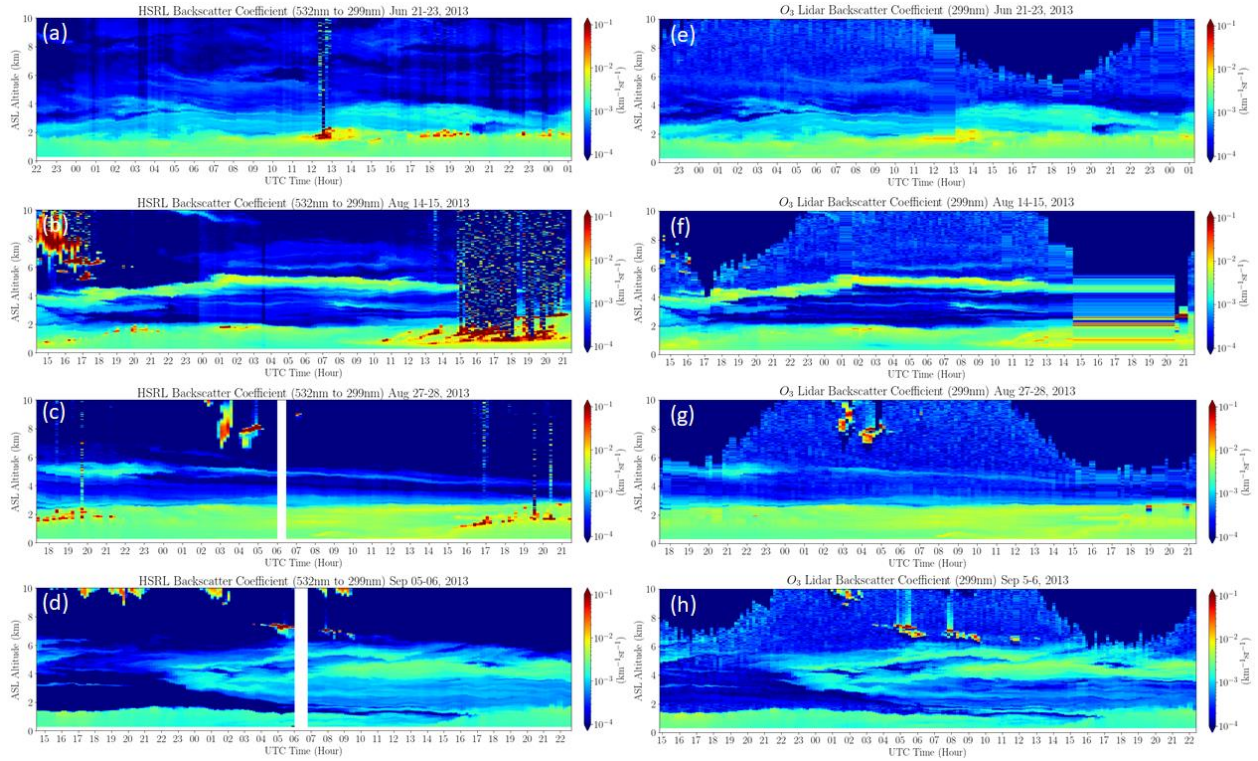
Figure 3. HSRL-converted aerosol backscatter coefficients (a, b, c, d) compared to RO$_3$QET lidar-derived aerosol backscatter coefficients at 299 nm (e, f, g, h), with 10-min temporal resolution and 30-m vertical resolution. The data was taken from 21–23 June (a, e), 14–15 August (b, f), 27–28 August (c, g), and 5–6 September (d, h) 2013. The HSRL-converted aerosol backscatter coefficients are scaled from the original retrievals at 532 nm to 299 nm using Eq. (1) and å$_\beta$=1.34.

627
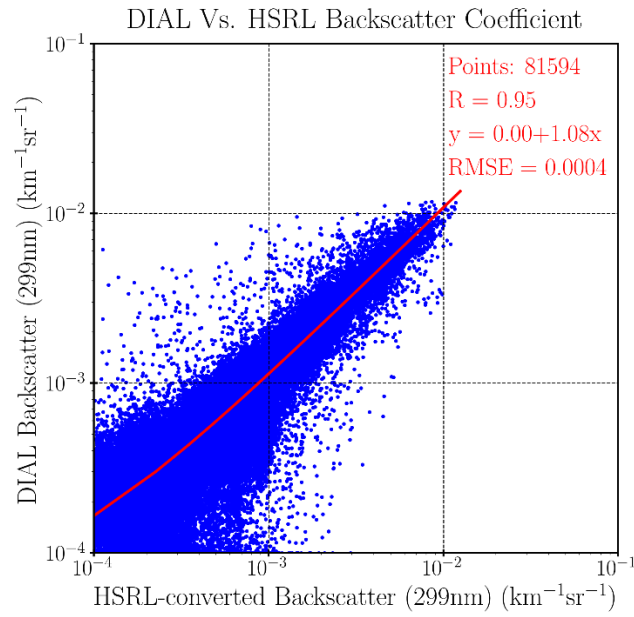
628    Figure 4. Regression of ozone lidar measured and HSRL-converted aerosol backscatter coefficients (interpolated to

629    299 nm with $\text{å}_\beta$=1.34) with 30-m vertical resolution and 10-min temporal resolution. The regression line is a little

630    curved in log scale because the intercept is not exactly zero.

631
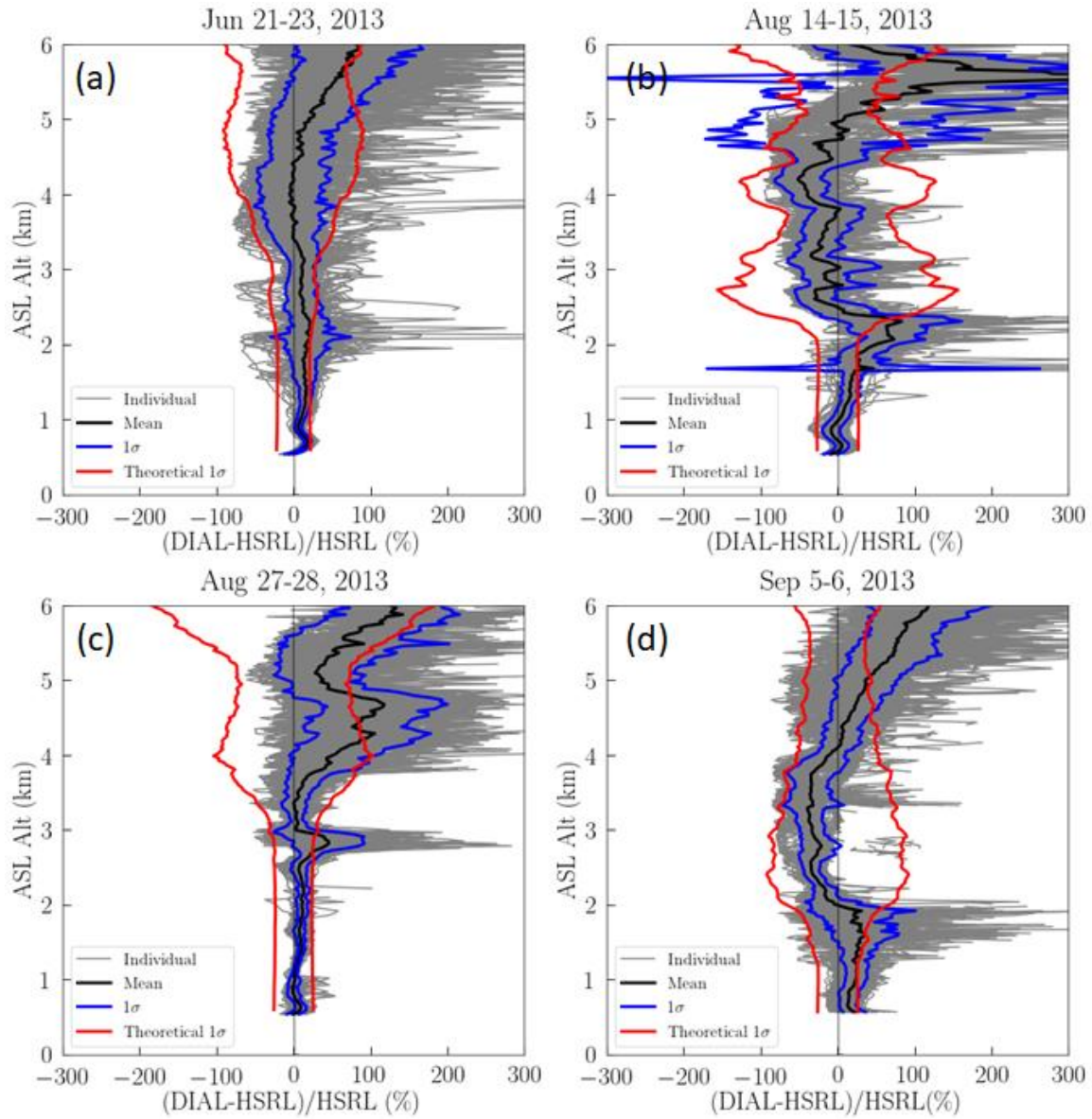
Figure 5. Relative differences between RO₃QET and HSRL-converted aerosol backscatter measurements, (RO₃QET-HSRL)/HSRL, made from (a) 21-–23 June, (b) 14-–15 August, (c) 27–28 August, and (d) 5–6 September, 2013. The gray and black lines represent the differences for the10-min individual aerosol backscatter profiles and their mean, respectively. The blue lines represent the actual 1 σ of the differences compared to the theoretical 1 σ (red lines) of the RO₃QET lidar aerosol measurement.

(a)

(b)
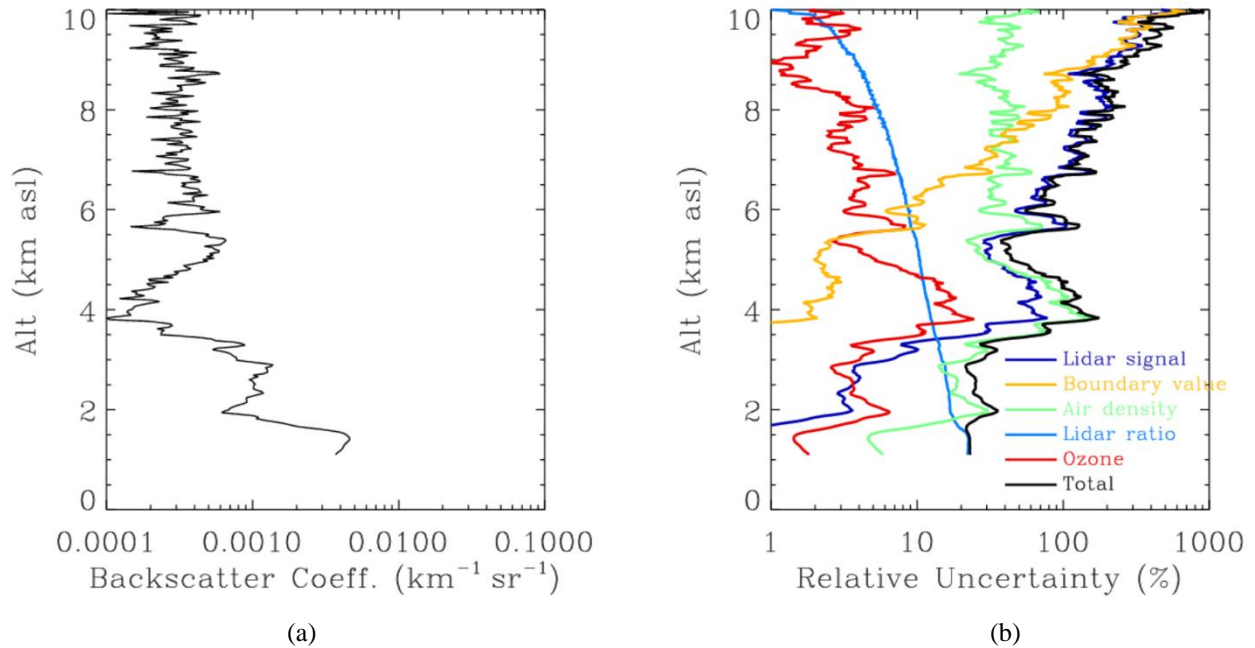
Figure B1. An example of (a) aerosol backscatter profile retrieved from 10-min ozone lidar data at about 8:30 UTC on 22 June 2013 and (b) the retrieval error budget for different uncertainty sources. The lidar data was from the Channel-3 receiving system which covers most of the measurement altitude range and was arbitrarily chosen for a cloud-free scenario.